Lithium Insertion into Vanadium Oxide Nanotubes: Electrochemical and Structural Aspects

Sara Nordlinder, Leif Nyholm, Torbjörn Gustafsson, and Kristina Edström*

Department of Materials Chemistry, Uppsala University, The Ångström Laboratory, Box 538, SE-751 21 Uppsala, Sweden

Received June 10, 2005. Revised Manuscript Received October 20, 2005

The electrochemical and structural aspects of lithium insertion into vanadium oxide nanotubes have been studied. Structural changes, induced as lithium was inserted between the vanadium oxide layers, were followed by in situ synchrotron X-ray diffraction recorded during potential steps. Two separate processes were identified: a fast decrease of the interlayer distance followed by a slow two-dimensional relaxation of the intralayer vanadium oxide structure. The nanotubes were synthesized using crystalline V_2O_5 as a precursor, instead of the normally used vanadium alkoxide, which produced a more cost-effective material with similar performance. Electrochemical measurements showed that surface processes, i.e., charge transfer and/or ohmic drop, were rate-controlling, as can be anticipated for the thin layer electrochemical conditions used in this study.

1. Introduction

Nanomaterials and their possible applications constitute a rapidly growing research field. Among the different geometric morphologies available, nanotubes and nanorods have attracted attention due to their anisotropic morphologies and abilities to host other materials.[1] Redox active vanadium oxide (VO_x) nanotubes were first synthesized by Spahr et al.[2] using a sol−gel method, followed by a hydrothermal step. Vanadium alkoxide was used as a precursor while primary amines were employed as structure-directing agents. Later, a low-cost synthesis route based on V_2O_5 or $VOCl_3$ precursors was presented.[3]

The vanadium oxide walls can be described as built up by flexible V_7O_{16} layers,[4,5] separated by templating molecules or ions, and the distance between the layers depends on the structure-directing agent.[6] A primary amine, dodecylamine, is normally used for the synthesis of the tubes. Alkali and transition metal ions, for example, Na^+, Ca^{2+}, Co^{2+}, and Ni^{2+}, can then replace the amine by an ion-exchange reaction.[7] However, if the embedded guests are completely removed, the structure collapses. Important to note is that V_7O_{16} is the ideal stoichiometry. The composition of the nanotubes most likely differs from this due to defects originating from the curved shape of the vanadium oxide layers. Therefore, the notation VO_x is hereafter used for the nanotubes. A single tube may contain up to 30 vanadium oxide layers, giving an outer diameter of up to 100 nm, and the tubes can reach 10 μm in lengh, depending on the synthesis conditions.[6]

Nanotubular vanadium oxide has been the subject of investigations in many areas including electronic properties,[8,9] optical properties,[10−12] and synthesis.[3,7,13−18] For battery applications, nanostructured materials can increase the performance of both cathodes and anodes.[19,20] Successful use of VO_x nanotubes as electrode material has been reported for Mn-exchanged nanotubes, which could be charged and discharged reversibly, giving capacities of 140 (mA h)/g.[21] Mo-doped tubes initially showed high capacities, close to 200 (mA h)/g, but the capacity decreased to 80−100 (mA h)/g after 50 cycles.[22] Sun et al.[23] explored disordered VO_x

* To whom correspondence should be addressed. Telephone: +46 18 471 3713. Fax: +46 18 513548. E-mail: kristina.edstrom@mkem.uu.se.

(1) Patzke, G. R.; Krumeich, F.; Nesper, R. *Angew. Chem., Int. Ed.* **2002**, *41*, 2446.
(2) Spahr, M. E.; Bitterli, P.; Nesper, R.; Müller, M.; Krumeich, F.; Nissen, H. U. *Angew. Chem., Int. Ed.* **1998**, *37*, 1263.
(3) Niederberger, M.; Muhr, H.-J.; Krumeich, F.; Bieri, F.; Günther, D.; Nesper, R. *Chem. Mater.* **2000**, *12*, 1995.
(4) Petkov, V.; Savalij, P. Y.; Lutta, S.; Whittingham, M. S.; Parvanov, V.; Shastri, S. *Phys. Rev. B* **2004**, *69*.
(5) Wörle, M.; Krumeich, F.; Bieri, F.; Muhr, H. J.; Nesper, R. *Z. Anorg. Allg. Chem.* **2002**, *628*, 2778.
(6) Krumeich, F.; Muhr, H.-J.; Niderberger, M.; Bieri, F.; Schnyder, B.; Nesper, R. *J. Am. Chem. Soc.* **1999**, *121*, 8324.
(7) Reinoso, J. M.; Muhr, H.-J.; Krumeich, F.; Bieri, F.; Nesper, R. *Helv. Chim. Acta* **2000**, *83*, 1724.
(8) Enyashin, A. N.; Ivanovskaya, V. V.; Makurin, Y. N.; Ivanovskii, A. L. *Phys. Lett. A* **2004**, *326*, 152.
(9) Enyashin, A. N.; Ivanovskaya, V. V.; Makurin, Y. N.; Volkov, V. L.; Ivanovskii, A. L. *Chem. Phys. Lett.* **2004**, *392*, 555.
(10) Cao, J.; Choi, J.; Musfeldt, J. L.; Lutta, S.; Whittingham, M. S. *Chem. Mater.* **2004**, *16*, 731.
(11) Webster, S.; Czerw, R.; Nesper, R.; DiMaio, J.; Xu, J. F.; Ballato, J.; Carroll, D. L. *J. Nanosci. Nanotechnol.* **2004**, *4*, 260.
(12) Xu, J. F.; Czerw, R.; Webster, S.; Carroll, D. L.; Ballato, J.; Nesper, R. *Appl. Phys. Lett.* **2002**, *81*, 1711.
(13) Chen, W.; Peng, J.; Mai, L.; Zhu, Q.; Xu, Q. *Mater. Lett.* **2004**, *58*, 2275.
(14) Chandrappa, G. T.; Steunou, N.; Cassaignon, S.; Bauvais, C.; Biswas, P. K.; Livage, J. *J. Sol-Gel Sci. Technol.* **2003**, *26*, 593.
(15) Chandrappa, G. T.; Steunou, N.; Cassaignon, S.; Bauvais, C.; Livage, J. *Catal. Today* **2003**, *78*, 85.
(16) Mai, L.; Chen, W.; Xu, Q.; Zhu, Q.; Han, C.; Peng, J. *Solid State Commun.* **2003**, *126*, 541.
(17) Chen, X.; Sun, X.; Li, Y. *Inorg. Chem.* **2002**, *41*, 4524.
(18) Bieri, F.; Krumeich, F.; Muhr, H.-J.; Nesper, R. *Helv. Chim. Acta* **2001**, *84*, 3015.
(19) Li, N.; Martin, C. R.; Scrosati, B. *J. Power Sources* **2001**, *97−98*, 240.
(20) Poizot, P.; Laurelle, S.; Grugeon, S.; Dupunt, L.; Tarascon, J.-M. *Nature* **2000**, *407*, 496.
(21) Dobley, A.; Ngala, K.; Shoufeng, T.; Zavalij, P. Y.; Whittingham, M. S. *Chem. Mater.* **2001**, *13*, 4382.

10.1021/cm051248w CCC: $33.50
Published on Web 12/21/2005

nanotubes and found that defect-rich tubes performed better than well-ordered tubes in a lithium battery. The positive effect was assigned to cracks in the tube walls and residual organic surfactant between the layers, favoring lithium diffusion. We have previously shown that VO_x nanotubes, ion-exchanged with Na^+, K^+, or Ca^{2+}, can be used in a Li-battery providing capacities comparable to those of other electrode materials.[24,25] In the latter studies, vanadium triisopropoxide was used as a precursor in the synthesis. In the present study, the synthesis of the nanotubes was based on V_2O_5, which gives a more cost-effective electrode material.

Little is known about the lithium insertion mechanism into the VO_x nanotubes. In the present report, we have made an effort to study this problem by using a combination of electrochemistry and XRD. The structural changes of the VO_x layers as a result of Li^+ insertion and extraction during potential steps were followed by time-resolved in situ synchrotron XRD. The advantage of performing diffraction experiments at synchrotron facilities is the very high intensity of the X-rays produced, which considerably shortens the measurement time. Previous in situ measurements of Na^+-VO_x nanotubes, using Cu Kα radiation, did not give satisfactory results as only the strongest peak, the 001 reflection originating from the VO_x layers, could be followed.[25] The reflections from the intralayer structure were hidden in the high background, created by the other cell components. It also proved difficult to interpret the final data from the measurements since the peaks were found to be broad. In summary, the previous study showed that only minor changes occurred in the intralayer distance as the electrode was discharged. Ex situ measurements performed in the same study showed that the 001 reflection was shifted to higher degrees in 2θ when the material was subjected to 100 cycles, indicating a decrease in the interlayer distance. Synchrotron XRD proved to be a more effective tool to study this material, allowing an exploration of the intralayer structure as well as the interlayer distances.

Information about the electrochemical response was obtained by using a combination of cyclic voltammetry, galvanostatic measurements, and chronoamperometry. For the thin laminate cells used in this study, diffusion will generally not be a rate-limiting step. Instead, charge-transfer kinetics and/or ohmic drop effects are expected to be the rate-controlling factors. In addition, cyclic voltammetric experiments were used to find the available potential window for the VO_x nanotubes.

2. Experimental Section

2.1. Synthesis. Vanadium oxide nanotubes were prepared as described by Niederberger et al.[3] using V_2O_5 (Aldrich) as a precursor and dodecylamine ($C_{12}H_{25}NH_2$, 99% Aldrich) as the structure-directing agent. The amine and the V_2O_5 powder, in the molar ratio 1:1, were dissolved in ethanol under an inert atmosphere and mixed for 2 h. Water was then added and the resulting gel was aged for 24 h. After aging, the product was transferred to an autoclave and kept at 180 °C for 7 days. The synthesis resulted in a black powder, consisting of VO_x nanorolls, which was washed in ethanol and dried at 80 °C overnight.

The ion exchange was performed as described by Krumeich et al.,[6] using $CaCl_2 \cdot 2H_2O$ (J. T. Baker Chemical Co.). The salt was dissolved in a 4:1 (by volume) mixture of ethanol and water. The VO_x tubes were then added so that the molar ratio of the salt to nanotubes was 4:1. The mixture was then stirred for 4 h. The product was finally washed and dried as described above.

The success of the synthesis was evaluated by XRD, and the results were compared with those of previous experiments (see for example ref 24).

2.2. Electrode Preparation. Electrodes were prepared by extrusion of a slurry containing 80 wt % $Ca^{2+}-VO_x$ nanotubes, 10 wt % carbon black (Shawinigan Black, Chevron), and 10 wt % ethylene propylene diene terpolymer binder (EPDM, 5 wt % in cyclohexane) onto aluminum foil. The thickness of the electrode film was 30−40 μm. Circular electrodes (20 mm in diameter) were dried under vacuum overnight inside an argon-filled glovebox (O_2/H_2O < 2 ppm) prior to use. The mass loading on the electrodes was ~1 mg/cm^2. This corresponds to a density of 0.25−0.33 g/cm^3, which implies that the electrode films were porous.

Two- or three-electrode cells were assembled inside the glovebox using the $Ca^{2+}-VO_x$ nanotubes as the working electrode and lithium foils as counter and reference electrodes. In the three-electrode arrangements, a small lithium reference electrode (diameter ~1 mm) was situated between two separators, close to the edge of the working electrode. The glass fiber separators used for the three-electrode cells were 250 μm thick. Hence, the distance between the working electrode and counter electrode was ~500 μm. For the in situ XRD measurements, the experimental setup only allowed two-electrode cells. These cells were prepared with thinner Solupor separators (~50 μm thick) to minimize the X-ray absorption. For all cells, the electrolyte was 1 M LiTFSI ($LiN(SO_2CF_3)_2$, Rhodia) in ethylene carbonate (EC):dimethyl carbonate (DMC) (both Selectipur, Merck) 2:1 by volume. The solvents were used as received whereas the LiTFSI salt was dried under vacuum at 120 °C for 24 h in the glovebox prior to use. The cell components were vacuum-sealed into polymer-coated aluminum pouches.

2.3. Electrochemical Measurements. Potentiostatic experiments were performed, with a three-electrode setup, using an EG&G Versastat II or a μAutolab, type II potentiostat. The latter was used to record the current transients in the potential step experiments, as well as the in situ electrochemistry and XRD measurements. A Digatron MTB testing unit was used in the galvanostatic charge and discharge experiments, all which were performed using two-electrode cells.

2.4. X-ray Diffraction. Powder synchrotron X-ray diffraction measurements were performed at beamline I711 at MAX Lab, Lund, Sweden, using a MarCCD 165 detector[26] and LaB_6 for calibration. Diffractograms of powder samples, measured in glass capillaries, and of separate electrodes were recorded with a wavelength of 0.9547 Å. In the potential step measurements, the wavelength used was 1.0885 Å. For the in situ measurements, a custom-made battery holder with transmission geometry was mounted on the goniometer head. The holder was tilted ±5° in the Phi angle during the 5 s long exposure. The batteries were connected to the μAutolab potentiostat, which controlled the electrochemistry during the

(22) Mai, L.-Q.; Chen, W.; Xu, Q.; Peng, J.-F.; Zhu, Q.-Y. *Chem. Phys. Lett.* **2003**, *382*, 307.
(23) Sun, D.; Kwon, C. W.; Baure, G.; Richman, E.; MacLean, J.; Dunn, B.; Tolbert, S. H. *Adv. Funct. Mater.* **2004**, *14*, 1197.
(24) Nordlinder, S.; Lindgren, J.; Gustafsson, T.; Edström, K. *J. Electrochem. Soc.* **2003**, *150*, E280.
(25) Nordlinder, S.; Edström, K.; Gustafsson, T. *Electrochem. Solid State Lett.* **2001**, *4*, A129.
(26) Cerenius, Y.; Ståhl, K.; Svensson, L. A.; Ursby, T.; Oskarsson, Å.; Albertsson, J.; Liljas, A. *J. Synchrotron Radiat.* **2000**, *7*, 203.

experiments. One diffractogram was recorded from the pristine battery, before the potential step was executed. During the potential steps, 60 frames (5 s exposure) were taken with approximately 10 s between each scan. Thereafter, one frame was measured every 10 min for 40 min followed by one frame every 30 min until either the current had dropped to at least 3 μA or 10700 s had passed (for the two largest steps).

The resulting CCD images were integrated using the "Fit2D" software (provided by Dr. A. Hammersley, ESRF, see ref 27). Calibrated wavelengths and detector positions were used.

2.5. Scanning Electron Microscopy. The surface morphology of the electrodes was examined by using a scanning electron microscope, SEM (LEO 1550 Gemini).

3. Results and Discussion

The success of the synthesis using V_2O_5 as a precursor was evaluated by XRD. Diffractograms of the as-synthesized and the ion-exchanged materials were compared to diffractograms of previously synthesized tubes, as well as to diffractograms reported in the literature (see e.g. ref 3, 6, and 7). Only reflections from the VO_x tubes were present in the diffractograms. Both precursors, V_2O_5 and vanadium alkoxide, produced the same final material and there was no difference in the electrochemical performance obtained in the two cases. The diffraction pattern for the $Ca^{2+}-VO_x$ nanotubes will be discussed further in section 3.3.

Electrodes were studied by SEM to confirm that the electrode preparation process did not damage the nanotubes. As can be seen in Figure 1, the tubular shape was indeed preserved. The image also shows the porous structure of the electrodes. Although it is seen that some nanotubes have aligned to form larger agglomerates, the nanotubes were generally well-separated.

3.1. Cyclic Voltammetry. The cyclic voltammogram for the first cycle with a three-electrode cell is shown in Figure 2a. Irreversible peaks at 3.06−2.90 V (all potentials are given vs Li/Li^+) could be seen on the first cathodic scan. These peaks could be connected to an initial structural change. There was, however, no evidence for irreversible structural reorganizations within the vanadium oxide layers that could be seen from the XRD data (presented in section 3.4). Another explanation for the irreversible peaks could be an extraction of water molecules or residual amines from the nanotubes occurring during the first discharge. Three broad peaks, at 2.56, 2.07, and 1.56 V, were also clearly visible in the cathodic region. On the anodic sweep, one peak appeared at 1.93 V while another was seen at 2.54 V. The latter had a shoulder at 2.72 V, which probably was coupled to the cathodic peak at 2.56 V.

The relationship between the peak current (I_p) and the sweep rate can generally give information about the diffusion of Li^+ in the electrolyte and electrode material. If semi-infinite diffusion is dominant, the peak current will be proportional to the square root of the sweep rate. For a finite diffusion distance, infinite rate of diffusion, the peak current will instead be proportional to the sweep rate.[28] The latter

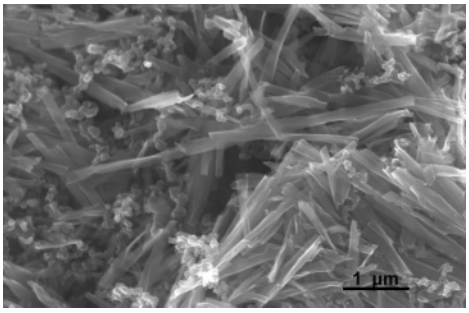

Figure 1. SEM image of an electrode made from Ca^{2+}-containing VO_x nanotubes.

relationship is expected for the thin laminate cell used in these investigations since the working electrode and the counter electrode were situated ~500 μm from each other and as low scan rates (between 0.05 and 0.8 mV/s) were used. To establish that the lithium insertion into the VO_x nanotubes behaved as a surface-confined process, a sweep rate study was performed using a three-electrode cell, which was scanned between 1.8 and 3.5 V. The anodic peak current (I_p) and peak potential (E_p) are plotted against the sweep rate in Figure 3. A linear relationship was indeed found between I_p and the sweep rate, confirming that the lithium insertion took place under thin layer electrochemical conditions.

The anodic peak potential (E_p) normally shifts toward more positive potentials (more negative potentials for a cathodic peak on the cathodic sweep) with increasing sweep rate if the process is controlled by the rate of charge transfer and/or IR drop effects.[28] In other words, the peak potential separation, ΔE_p, increases with increasing scan rate. ΔE_p will be constant only in a diffusion-controlled system with fast electron transfer, in the absence of significant IR drop effects. In the presence of a significant ohmic drop, the peak potential is expected to depend linearly on the scan rate (under thin layer electrochemical conditions) since the peak current should be proportional to the scan rate. As seen in Figure 3, E_p did shift toward more positive potentials for increasing scan rates. The relationship between E_p and the sweep rate was found to be nonlinear, although I_p depended linearly on the scan rate. This implies that the lithium insertion process is mainly kinetically controlled, except possibly at the lowest scan rates.

To determine the available potential window of the electrodes, the three-electrode cells were submitted to scans between different potential limits. The smallest potential window was chosen to be between 3.2 and 1.8 V. For every cycle, the potential window was then increased by 0.1 V in each direction until the potentials 3.8 and 1.2 V were reached. All scans were made consecutively on the same battery. Figures 2b and 2c show voltammograms for the potential windows: 3.2−1.8, 3.4−1.6, 3.6−1.4, and 3.8−1.2 V, respectively. The shapes of the peaks differed on the cathodic and the anodic scans. The anodic peak, centered at ~2.5 V, was larger than the two cathodic peaks observed. This asymmetry, which may be due to different mechanisms for lithium insertion and extraction, will be discussed further in section 3.3.

(27) http://www.esrf.fr/computing/scientific/FIT2D/2005.
(28) Hjelm, A.-K.; Lindbergh, G.; Lundqvist, A. *J. Electroanal. Chem.* **2001**, *506*, 82.

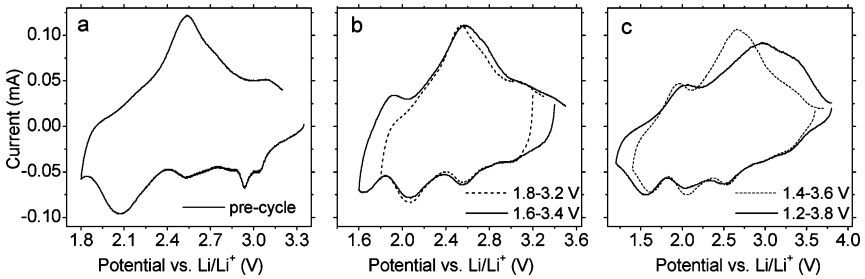

Figure 2. Cyclic voltammograms for the first cycle (a) and for four different potential windows (b, c). All scans were made consecutively on the same cell and the sweep rate was 0.05 mV/s.

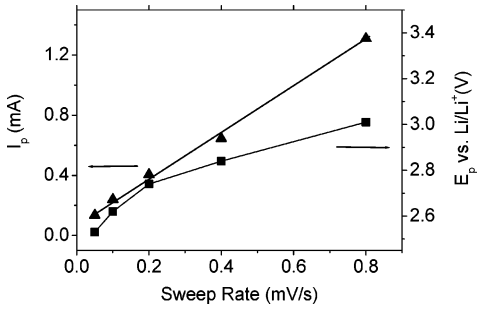

Figure 3. Anodic peak current (▲) and peak potentials (■) plotted as a function of the sweep rate. The sweep rates used were 0.05, 0.1, 0.2, 0.4, and 0.8 mV/s.

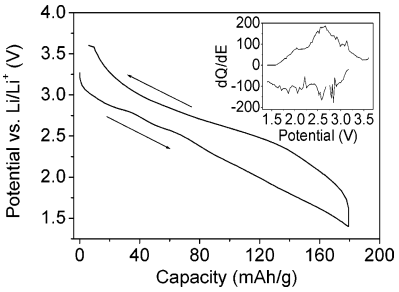

Figure 4. First cycle galvanostatic curves for a Ca−VO_x electrode. The potential cutoffs were set to 3.6 and 1.4 V. Current loading: 25 mA/g, corresponding to one complete discharge in 7 h. The inset shows the derivative, d*Q*/d*E*, of the galvanostatic curves.

For the largest potential window (1.2−3.8 V), the shapes of the anodic peaks differed substantially from those seen with the other potential limits. The anodic peaks were broader and shifted to more positive potentials. Above 3.6 V, LiTFSI is known to corrode the aluminum foil used as the current collector.[29] However, there was no evidence of such a process in this study. Such a reaction would have given rise to increased currents in this potential range. The broadening of the peaks seen with the largest potential window may also have been affected by an aging effect due to the repeated cycling. In a series of voltammetric scans between 3.6 and 1.8 V (data not shown), both the anodic and the cathodic peaks were broadened and slightly shifted toward more negative (cathodic scans) and more positive (anodic scans) potentials over 23 cycles. The latter could be explained by a loss of crystallinity in the vanadium oxide sheets.[30] However, the shift in the peak potential was not as prominent as in the voltammograms recorded with the largest potential window, suggesting a different effect as in the voltammograms within the latter case. The observed shift in the anodic peak potential was more likely due to a resistance of the reduced vanadium oxide layers to re-adopt their original structure. The use of the low potential limit (1.2 V) could generate considerable amounts of V^{3+}, initiating side reactions and/or phase transitions detrimental to the battery performance. According to a previous XPS study, V^{3+} is formed already at potentials around 2.0 V. At 1.8 V, three vanadium oxidation states were found to coexist with the distribution: 23% V^{5+}, 51% V^{4+}, and 26% V^{3+}.[31] The amount of V^{3+} should naturally be even higher at a potential of 1.2 V. The differently shaped voltammograms seen when using cathodic potential limits below 1.3 V could hence be the result of a distortion of the VO_x structure.

3.2. Chronopotentiometry. Galvanostatic measurements, performed with two-electrode cells, gave rise to weak plateaus at 2.8 V and 2.6 V on an otherwise nearly linear potential versus time curve (Figure 4). This is in agreement with the earlier observed behavior of VO_x nanotubes.[24,25] The absence of well-defined plateaus indicates the absence of the formation of discrete phases. The inset in Figure 4 shows the derivative, d*Q*/d*E*, for the discharge and charge. In accordance with the shape of the voltammograms (Figure 2), there are significant differences between the shapes of the charge and discharge curves. The charge curve contains one large peak, while the discharge curve exhibits several minor peaks. The galvanostatic curves hence also exhibit asymmetric features, which are analogous to those seen in the cyclic voltammograms. This asymmetry indicates that the charge and discharge of the active material involve significant structural rearrangements.

Specific capacities for the different potential spans discussed above over 30 cycles are shown in Figure 5. As expected, the capacity increased if the potential window was extended. However, if a potential window between 1.2 V and 3.8 V was used, the capacity was found to decrease with time, most likely due to destructive side reactions and/or phase transitions. The initial high capacity (∼270 (mA h)/g) decreased after the first six cycles and reached a value of 125 (mA h)/g after 30 cycles. The theoretical capacity can be estimated at ∼370 (mA h)/g assuming that the vanadium is reduced from the presumed average oxidation state +4.28 to the oxidation state +3.00 (based on the insertion of 9 Li^+

(29) Krause, L. J.; Lamanna, W.; Summerfield, J.; Engle, M.; Korba, G.; Loch, R.; Atanasoski, R. *J. Power Sources* **1997**, *68*, 320.
(30) Spahr, M. E.; Stoschitzki-Bitterli, P.; Nesper, N.; Haas, O.; Novák, N. *J. Electrochem. Soc.* **1999**, *146*, 2780.
(31) Nordlinder, S.; Augustsson, A.; Schmitt, T.; Guo, J.; Duda, L. C.; Nordgren, J.; Gustafsson, T.; Edström, K. *Chem. Mater.* **2003**, *15*, 3227.
(32) Zavalij, P.; Whittingham, M. S. *Acta Crystallogr.* **1999**, *B55*, 627.

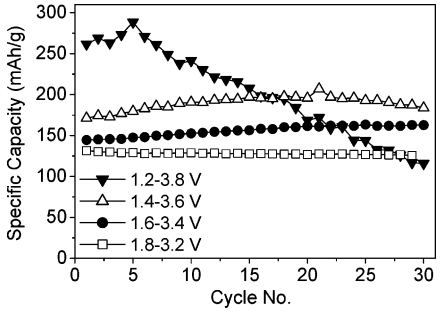

Figure 5. Charge capacity over 30 cycles for varying cutoff potentials. The current loading was 25 mA/g, corresponding to a complete discharge in 7 h.

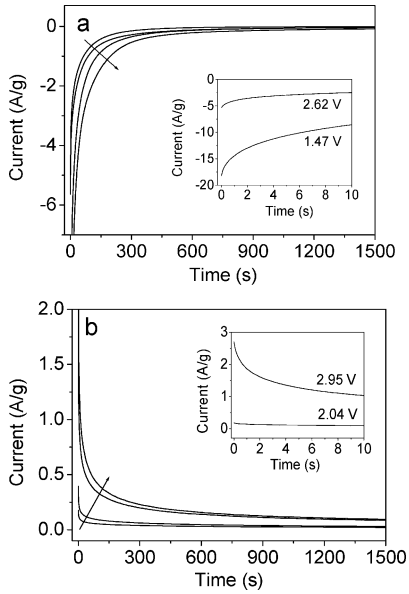

Figure 6. Current−time transients for cathodic (a) and anodic (b) potential steps. The cathodic steps were made to 2.62, 2.38, 1.91, and 1.47 V, respectively. The arrow indicates decreasing potential. The anodic steps were made to 2.04, 2.13, 2.78, and 2.95 V, respectively. The arrow indicates increasing potentials. The insets display the 0−10 s time range for selected potential steps (indicated in the figure). All currents were normalized to the amount of the active material on the individual electrodes.

to the ideal stoichiometry $M_2 + CaV_7O_{16}$, M = metal ion). A reversible reduction to V^{3+} is, however, not likely since this would involve large structural changes in the VO_x layers.

Summarizing the results of the cyclic voltammetric and galvanostatic measurements discussed above, the battery can be discharged to about 1.5 V, but not further than 1.3 V, and charged to 3.5 V while maintaining reversible operation of the battery.

3.3. Chronoamperometry. To facilitate a distinction between potential and time effects and to enable studies of the structure of the nanotubular material at a range of specified potentials, cathodic potential steps were made from the open circuit potential (OCP ∼3.4 V), to seven different potentials: 2.62, 2.47, 2.38, 1.98, 1.91, 1.55, and 1.47 V. Anodic steps, to 2.04, 2.13, 2.78, and 2.95 V, were likewise made using electrodes that previously had been discharged with a current loading of 10 mA/g (corresponding to one complete discharge in 24 h) and equilibrated at 1.3 V for approximately 4 days. The potentials were chosen to study the cathodic and anodic peaks seen in the cyclic voltammograms. All potential step experiments were performed on different batteries.

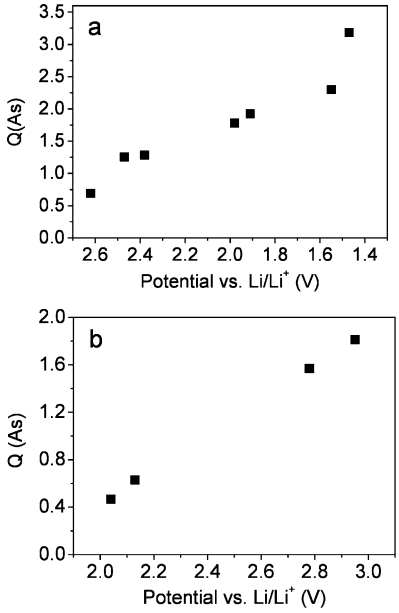

Figure 7. Charge (■) for (a) the cathodic potential steps and (b) the anodic potential steps, calculated from the current−time transients and the amount of the active electrode material. The cathodic steps were performed from OCP (∼3.4 V) and the anodic from a discharged cell equilibrated at 1.3 V.

Table 1. Calculated Number of Transferred Li^+ in Each Potential Step

	E step (V)	Number of transferred Li^+
discharge	2.62	1.7
	2.47	2.6
	2.38	3.2
	1.98	4.2
	1.91	4.5
	1.55	4.3
	1.47	7.7
charge	2.04	1.0
	2.13	1.4
	2.78	4.4
	2.95	5.1

The resulting current transients are shown in Figure 6 for the cathodic (a) and anodic (b) potential steps. For clarity, only a few of the cathodic transients have been included in the graph. All measurements were performed on separate batteries, meaning that first cycle effects may have influenced the results. The transients, which exhibit non-Cottrellian shapes, as expected for these thin laminate cells, were used to determine the charge passed during each potential step. The insertion of Li^+ into the vanadium oxide nanotubes can proceed in two ways. In the first case, discrete phases are formed as the amount of lithium in the material increases. The other alternative involves the formation of a solid solution of Li_yVO_x. If the intercalation of lithium into the vanadium oxide results in a solid solution, there should be a linear relationship between the potential and the charge associated with that potential step. Such a plot can therefore be compared with the galvanostatic charge/discharge curves seen in Figure 4. Figure 7 show plots of the charge passed during the individual cathodic (a) and anodic (b) steps. The asymmetry, seen in both the voltammograms (Figure 2) and chronopotentiograms (Figure 4), is clearly present also in Figure 7. While the plot for the anodic steps (Figure 7b) was linear, as for the charging or discharging of a capacitor,

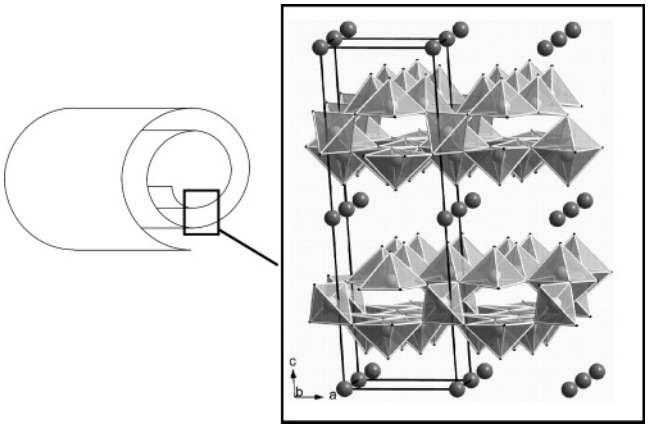

Figure 8. Schematic picture showing the scroll-like structure of the VO_x nanotubes and the structural model for the ideal V_7O_{16} interlayer structure viewed along the *b*-axis. The atomic coordinates from ref 5 were used. The Ca^{2+} ions are represented by gray spheres between the VO_x layers. Note that the positions of the Ca^{2+} ions are arbitrary.

the shape of the cathodic plot (Figure 7a) was more irregular. For the largest cathodic step, to 1.47 V, the charge was found to be higher than expected, possibly due to a slightly different amount of active material on the electrodes. Thinner electrodes, with less active material, may allow a more effective utilization of the active material, thereby producing higher capacities compared to electrodes with a higher mass loading. Another explanation for the higher charge of the last point in Figure 7a, could, however, be that another reduction process becomes possible at this potential. Structural reorganizations at potentials below 1.5 V could produce a different environment for the Li^+. This could in turn allow additional reductions of the vanadium oxide. For example, a more defect-rich structure could host additional Li^+, as has been shown by Sun et al.[23] Table 1 contains the calculated number of Li^+ transferred in each potential step together with the average vanadium oxidation states. The calculations of the oxidation states were based on the ideal starting composition CaV_7O_{16}, which has an average oxidation state of +4.28. Due to defects originating from the curvature of the vanadium oxide layers, the average oxidation state for the synthesized nanotubes will probably be somewhat different from the ideal structure. However, the ideal stoichiometry is used here to give an estimate of the changes in oxidation state occurring as Li ions are inserted and extracted. The oxidation states for the anodic steps are not possible to estimate since the initial oxidation states for the discharge samples are unknown. After the potential step from OCP to 1.47 V, the oxidation state of the vanadium is close to +3, which implies that a significant part of the material must be in the +3 oxidation state.

3.4. In Situ XRD. To follow the structural changes during a potential step, in situ XRD was performed. Since a synchrotron source was used, time-resolved measurements could be made with a resolution (i.e., time between two consecutive diffractograms) of ~15 s, which made it possible to closely follow the evolution of the diffraction pattern for the VO_x nanotubes with time during the potential steps.

The building blocks of the V_7O_{16} layers in the nanotubes are double layers of square pyramidal VO_5 units with embedded VO_4 tetraedra (Figure 8). The five-coordinated

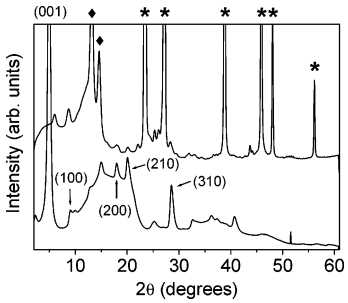

Figure 9. Powder X-ray diffractograms of a $Ca-VO_x$ powder (bottom) and a $Ca-VO_x$ electrode enclosed in the polymer laminated aluminum pouch (top). The additional reflections in the latter originate from the aluminum current collector, the binder, and the pouch materials. Diffraction peaks from aluminum and the binder material are marked with (*) and (♦), respectively. The reflections of interest are marked with their *hkl*-assignments in the powder pattern.

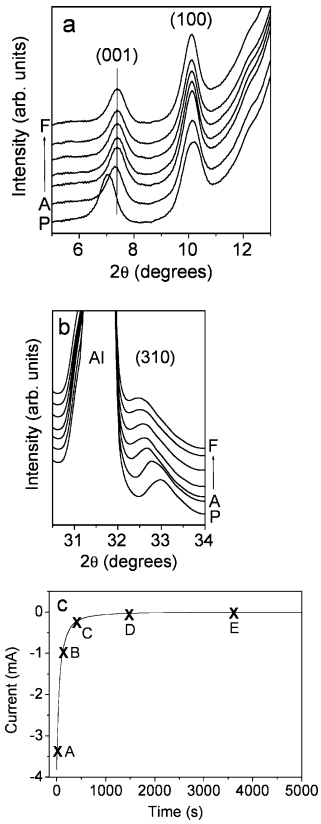

Figure 10. In situ XRD measurements during the potential step from OCP to 2.15 V: (a) the 001 and 100 reflections, (b) the 310 reflection, and (c) the corresponding current transient (**X** marks the positions of the diffractograms). The diffractograms were recorded after (from bottom to top): (P) pristine battery, (A) 2 min (120 s), (B) 7 min (420 s), (C) 14 min 30 s (900 s), (D) 25 min (1500 s), (E) 1 h (3600 s), and (F) 2 h (not shown in 10c).

vanadium atoms can also be seen as coordinated in a distorted octahedral arrangement with one long V−O bond (~2.4 Å). Short V−O bonds are directed toward the interlayer spacing, coordinating the embedded guests. Since the space within the VO_x layers is too small to allow migration of lithium ions through these layers, all Li^+ will end up between the VO_x sheets and coordinate to the vanadyl oxygens.

Figure 9 shows the powder diffraction patterns for the $Ca^{2+}-VO_x$ nanotubes and an electrode enclosed in a polymer-coated aluminum pouch, respectively. The latter diffactogram contained peaks from the EPDM binder (13−15° in 2θ) and from aluminum (six strong peaks $2\theta > 25°$)

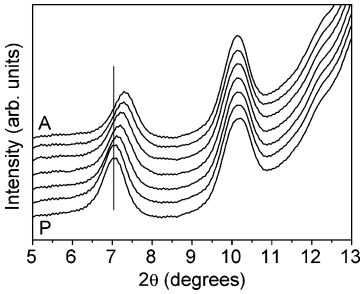

Figure 11. In situ XRD patterns for the 001 and 100 reflections during the potential step from OCP to 2.15 V, showing the changes during the first 2 min. The diffractograms were recorded after (from bottom to top) 1−5 s, 15 s, 30 s, 45 s, 1 min 15 s, and 2 min (diffractogram A is the same as in Figure 10a).

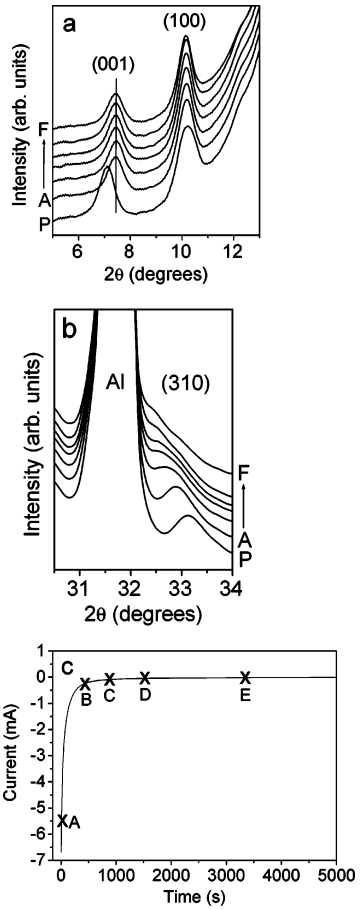

Figure 12. In situ XRD measurements during the potential step from OCP to 1.71 V: (a) the 001 and 100 reflections, (b) the 310 reflection, and (c) the corresponding current transient (**X** marks the positions of the diffractograms). The diffractograms were recorded after (from bottom to top) (P) pristine battery, (A) 2 min (120 s), (B) 7 min (420 s), (C) 14 min 30 s (900 s), (D) 25 min (1500 s), (E) 1 h (3600 s), and (F) 2 h (not shown in 12c).

as well as several minor peaks originating from aluminum oxide and materials in the polymer-coated Al pouches. The 001 peak is normally the strongest reflection for the $Ca^{2+}-VO_x$ nanotubes, and the corresponding *d*-value gives the distance between the VO_x layers. Peaks observed at $2\theta > 10°$ are *hk*0 reflections originating from the structure within the VO_x layers. These reflections did not change when the embedded guests changed. Consequently, the intralayer structure was, to a first approximation, independent of the guest ion. The intensity ratios between the 001 reflection and the *hk*0 reflections were clearly different for the electrode

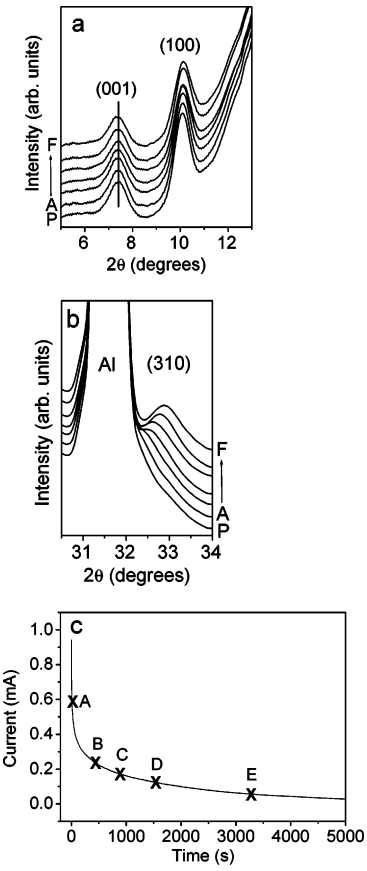

Figure 13. In situ XRD measurements during the potential step from 1.6 V to 2.78 V: (a) the 001 and 100 reflections, (b) the 310 reflection, and (c) the corresponding current transient (**X** marks the positions of the diffractograms). The diffractograms were recorded after (from bottom to top) (P) pristine battery, (A) 2 min (120 s), (B) 7 min (420 s), (C) 14 min 30 s (900 s), (D) 25 min (1500 s), (E) 1 h (3600 s), and (F) 2 h (not shown in 13c).

compared to those for the pure powder. The preferred orientation of the nanotubes in the electrode film may have caused this altered intensity distribution. Unfortunately, the $Ca^{2+}-VO_x$ nanotubes only gave rise to weak and broad peaks in comparison with the other cell components. Significant changes in the diffraction pattern could, however, be seen as the material was charged or discharged.

Two regions of the $Ca^{2+}-VO_x$ diffractogram will be discussed below: (a) the 001 and 100 peaks at $2\theta \sim 7°$ and $\sim 10°$, respectively and (b) the 310 peak at $2\theta \sim 33°$. The other *hk*0 reflections showed similar behaviors, but they were difficult to analyze properly and were therefore not included. The bottom patterns (marked P) in Figures 10−13 were obtained with the pristine battery, prior to the potential step. Pattern A was recorded 2 min after the potential step, and the corresponding position is marked in the current transients. The successive diffractograms were recorded after (B) 7 min, (C) 14 min 30 s, (D) 25 min, (E) 1 h, and (F) 2 h (not marked in the transient).

There was a slight mismatch between the powder pattern and the pattern from the electrode at low angles, in that the 001 reflection was shifted to higher 2θ for the electrode. The shift corresponds to a change in interlayer distance from 10.9(1) Å for the powder to 9.1(1) Å for the electrode. Possibly a contraction of the VO_x layers was induced by a removal of embedded water and/or a rearrangement of the

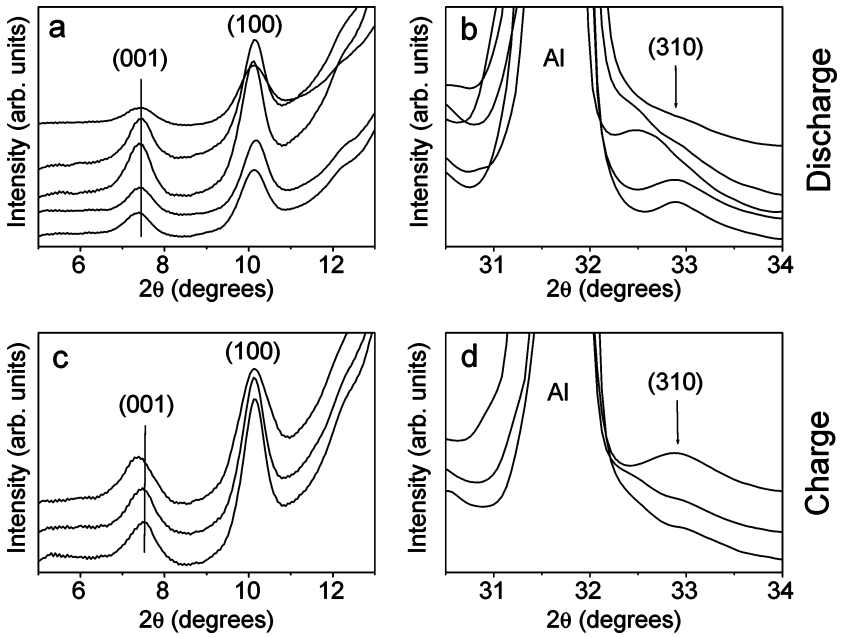

Figure 14. In situ X-ray diffractograms ($\lambda = 1.0886$ Å) for (a, b) the cathodic potential steps from OCP to 2.62, 2.47, 2.15, 1.71, and 1.52 V (from bottom to top) and (c, d) anodic (charge) potential steps from ~1.5 to 1.87, 2.04, and 2.78 V (from bottom to top). The frames are recorded when $|I(t)| < 4$ μA.

Ca^{2+} caused by the heating step during electrode preparation (all electrodes were heat-treated at 120 °C overnight). The interlayer distance decreased further to 8.79(5) Å as the electrode was incorporated into a battery as can be seen for the pattern marked P in Figure 10a. Interactions with solvent molecules and/or Li^+ from the electrolyte could therefore have caused the additional compression of the VO_x layers. Li^+ have a smaller ionic radius than Ca^{2+} (76 and 100 pm, respectively), which means that an exchange of Ca^{2+} for Li^+ would result in a decreased interlayer distance. The amines cannot be spontaneously exchanged for Li^+ during the commonly used ion-exchange process.[7] However, it is possible that the environment in the cell, where aprotic solvents are coordinated to the Li^+, favors such a substitution. It is important to note that all pristine batteries had the same *d*-value for the 001 reflection. When a potential was applied, the 001 reflection exhibited a shift from 7.1° to 7.4° during the first 2 min corresponding to a decrease in interlayer distance from 8.79(5) to 8.43(5) Å. This can be seen in Figures 10a, 12a, and 13a. Considering the diffraction patterns recorded before 2 min (Figure 11), it could seen that the shift of the 001 peak, and consequently the contraction of the VO_x layers, occurred gradually and not in a single step. On the other hand, the 100 reflection did not move at all during the potential step.

A shift of the 310 reflection from 33.0° to a maximum of 32.5°, for the cathodic potential steps occurred gradually during a much longer time period (Figures 10b and 12b). The size of the shift was dependent on the end potential, i.e., the amount of inserted Li^+. A reverse shift in the 310 reflection was found for the anodic steps. As shown in Figure 13b, the peak finally ended up at 32.9°. Surprisingly, the 001 peak did not shift back to lower 2θ (Figure 13a), and it is hence possible that this decrease in the interlayer distance is a first-cycle effect.

Figures 14a and 14b contain diffraction patterns for five cathodic steps from OCP to 2.62, 2.47, 2.15, 1.71, and 1.52 V, respectively (from bottom to top in the figure) recorded when the current had dropped below 4 μA. The latter occurred after 1−2 h depending on the size of the potential step (ΔE_{step}). This implies a system close to equilibrium. The 001 reflection remained at 7.4° in 2θ independent of the size of the potential step (Figure 14a). For the 310 reflection, an increasing shift could be detected as ΔE_{step} was increased. As seen in Figure 14b, the 310 reflection finally merged into the aluminum peak.

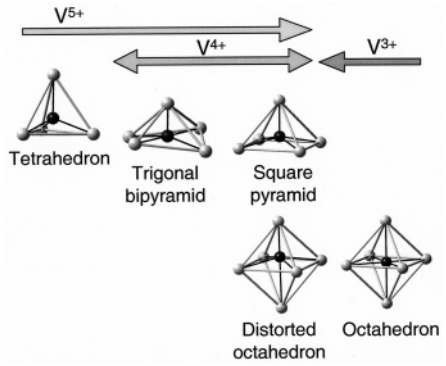

Figure 15. Different vanadium−oxygen coordination polyhedra. The figure is based on Figure 1 in ref 32.

Diffractograms obtained for the three anodic steps, from ~1.5 to 1.87, 2.04, and finally to 2.78 V (from bottom to top in the figure), are shown in Figures 14c and 14d. Only a very small shift of the 001 reflection toward lower 2θ could be detected for the largest anodic step (Figure 14c). It was also found that the 310 peak returned to 32.9° after the largest anodic step (Figure 14d).

Summarizing the results from the in situ diffraction study, it becomes clear that there are at least two processes occurring as the Li^+ enter into the VO_x nanotubes. Initially, Li^+ are inserted between the VO_x layers. This is a fast process, which occurs in a fairly disordered way, causing the interlayer distance to decrease. Second, the Li^+ diffuse to find a favorable site in the interlayer spacing. This affects

the intralayer VO_x structure. The reduction of vanadium is accompanied by an increase in its coordination number. Different possible coordination polyhedra are shown in Figure 15. Tetrahedral vanadium is always in the +5 oxidation state, while vanadium in the +3 oxidation state is always octahedrally coordinated. Vanadium in the +5 and +4 oxidation states can adopt three types of five-coordinated arrangements: trigonal bipyramid, square pyramid, and distorted octahedral arrangement. Initially, the VO_x sheets are composed of double layers of square pyramids separated by tetrahedra (Figure 8). The average oxidation state for vanadium in the ideal stoichiometry, CaV_7O_{16}, is +4.28, which suggests that there are two V^{5+} and five V^{+4} in one formula unit. The calculated number of Li^+ inserted during each potential step, based on the charges in Figure 7, is shown in Table 1. The anomaly for the step to 1.55 V is probably due to the use of a slightly thicker electrode in that specific cell.

When lithium is inserted between the sheets, vanadium is reduced from V^{5+} to V^{4+} and from V^{4+} to V^{3+}. The formation of regular octahedra around vanadium in the +3 oxidation state would cause buckling of the VO_x layers since the vanadium atoms will need to alter their positions. This will in turn lead to changes in the cell parameters, thereby producing a shift in the intralayer reflections, as seen by XRD. The buckling will be dependent on the absolute oxidation state of vanadium, and this is reflected in the potential dependence of the 310 peak. Reducing the material to 1.2 V resulted in a decreased electrochemical performance. If a large amount of V^{5+} in tetrahedral coordination is reduced, the structure will be significantly altered. It is possible that the tetraherally coordinated vanadium, situated between the vanadium oxide double layers, is the key to the successful use of the present material in electrodes. Evidently, the reorganization of the layers occurring below 1.2 V does not allow Li^+ to be inserted reversibly to the same extent as the original structure.

The asymmetry seen in the electrochemical data for the charge and reduction and oxidation processes can be due to different lithium insertion and removal processes. This can be understood by considering the slow reorganization of the VO_x structure occurring as Li^+ diffuse to their final sites. The surroundings of the Li^+ will be different at the end of the discharge compared to those when the discharge was initiated. Therefore, Li^+ transport from the sites may follow a different process, giving rise to the mismatch seen between the discharge and charge curves. However, since we can only use a limited number of reflections, it is difficult to elaborate further on the precise lithium insertion/extraction process.

4. Conclusions

According to results from the electrochemical measurements, lithium enters the VO_x nanotubes in a solid solution-like process. This is confirmed by XRD results, where a gradual peak shift is seen in the diffractograms. There are at least two processes occurring as Li^+ enters the material: a fast decrease of the interlayer distance, followed by a slower two-dimensional relaxation of the structure within the VO_x layers. The electrochemical measurements indicate that the lithium insertion process is different from the extraction process, which can be due to a reorganization of the structure due to the insertion of Li^+ between the VO_x layers.

To approach the theoretical capacity for $Ca^{2+}-VO_x$ nanotubes, the low potential limit must be set below 1.5 V but not lower than 1.3 V. Using a too cathodic potential limit appears to induce phase transitions that reduce the cell performance considerably. The rate-controlling processes in a real battery are expected to be charge transfer and/or ohmic drop effects, in agreement with the experimental results.

Acknowledgment. This work has been supported by The Swedish Research Council (VR) and The Göran Gustafsson's Foundation (GGS). Dr. Yngve Cerenius (MAX Lab, Lund, Sweden) and Wendy Haglund (Uppsala University) are acknowledged for help with the synchrotron measurements and SEM characterization, respectively. S.N. thanks Dr. J. Höwing (Uppsala University, Sweden) for fruitful discussions.

CM051248W